# Microwave Brightness Temperatures from Tilted Convective Systems

YE HONG

*Caelum Research Corporation, Rockville, Maryland*

JEFFREY L. HAFERMAN

*Fleet Numerical Meteorology and Oceanography Center, Monterey, California*

WILLIAM S. OLSON

*Joint Center for Earth Systems Technology, University of Maryland Baltimore County, Baltimore, Maryland*

CHRISTIAN D. KUMMEROW

*NASA Goddard Space Flight Center, Greenbelt, Maryland*

(Manuscript received 2 January 1999, in final form 19 June 1999)

ABSTRACT

Aircraft and ground-based radar data from the Tropical Ocean and Global Atmosphere Coupled Ocean–Atmosphere Response Experiment show that convective systems are not always vertical. Instead, many are tilted from vertical. Satellite passive microwave radiometers observe the atmosphere at an oblique angle. For example, the Special Sensor Microwave Imager on Defense Meteorological Satellite Program satellites and the Tropical Rainfall Measurement Mission (TRMM) Microwave Imager (TMI) on the TRMM satellite view at an incident angle of about 50°. Thus, the brightness temperature measured from one direction of tilt may be different than that viewed from the opposite direction because of the different optical path. This paper presents an investigation of passive microwave brightness temperatures upwelling from tilted convective systems.

To account for the effect of tilt, a 3D backward Monte Carlo radiative transfer model has been applied to a simple tilted cloud model and a dynamically evolving cloud model to derive the brightness temperature. The radiative transfer results indicate that brightness temperature varies when the viewing angle changes because of the different optical path. The tilt increases the displacements between the high 19-GHz brightness temperature ($Tb_{19}$) due to liquid emission from the lower level of cloud and the low 85-GHz brightness temperature ($Tb_{85}$) due to ice scattering from the upper level of cloud. As the resolution degrades, the difference of brightness temperature due to the change of viewing angle decrease dramatically. The displacement between $Tb_{19}$ and $Tb_{85}$, however, remains prominent.

The successful launch and operation of the TRMM satellite provide an opportunity to examine tilted convective systems using collocated radar and radiometer data. TMI observations of tilted systems indicate that displacement between $Tb_{19}$ and $Tb_{85}$ can be as far as 100 km. Such displacement not only poses a problem to rainfall retrieval algorithms that use only scattering information but also causes large uncertainty in rainfall retrieval from multichannel retrieval algorithms. This study suggests that combined radar and radiometer data are needed to reduce the effect of tilt and to improve surface rainfall retrieval.

## 1. Introduction

Measurement of tropical rainfall is very important for understanding the hydrological cycle and its role in the global climate system. Satellite observation of tropical rainfall is necessary because of the huge extent of oceans in the Tropics. In comparison with visible/infrared observations, passive microwave observations provide better physical information for estimating surface rainfall because microwaves can penetrate clouds and interact directly with hydrometeors at lower levels. Upwelling passive microwave brightness temperatures are determined by the surface emissivity and the vertical distributions of ice and liquid contents of clouds. At low microwave frequencies (<37 GHz), the brightness temperature responds mostly to emission from rain and cloud liquid, and thus the observed brightness temperature increases over the radiometrically cold ocean. In contrast, at high frequencies (>37 GHz), the brightness temperature responds mainly to scattering from cloud

*Corresponding author address:* Ye Hong, NASA/GSFC, Code 912, Greenbelt, MD 20771.
E-mail: yhong@agnes.gsfc.nasa.gov

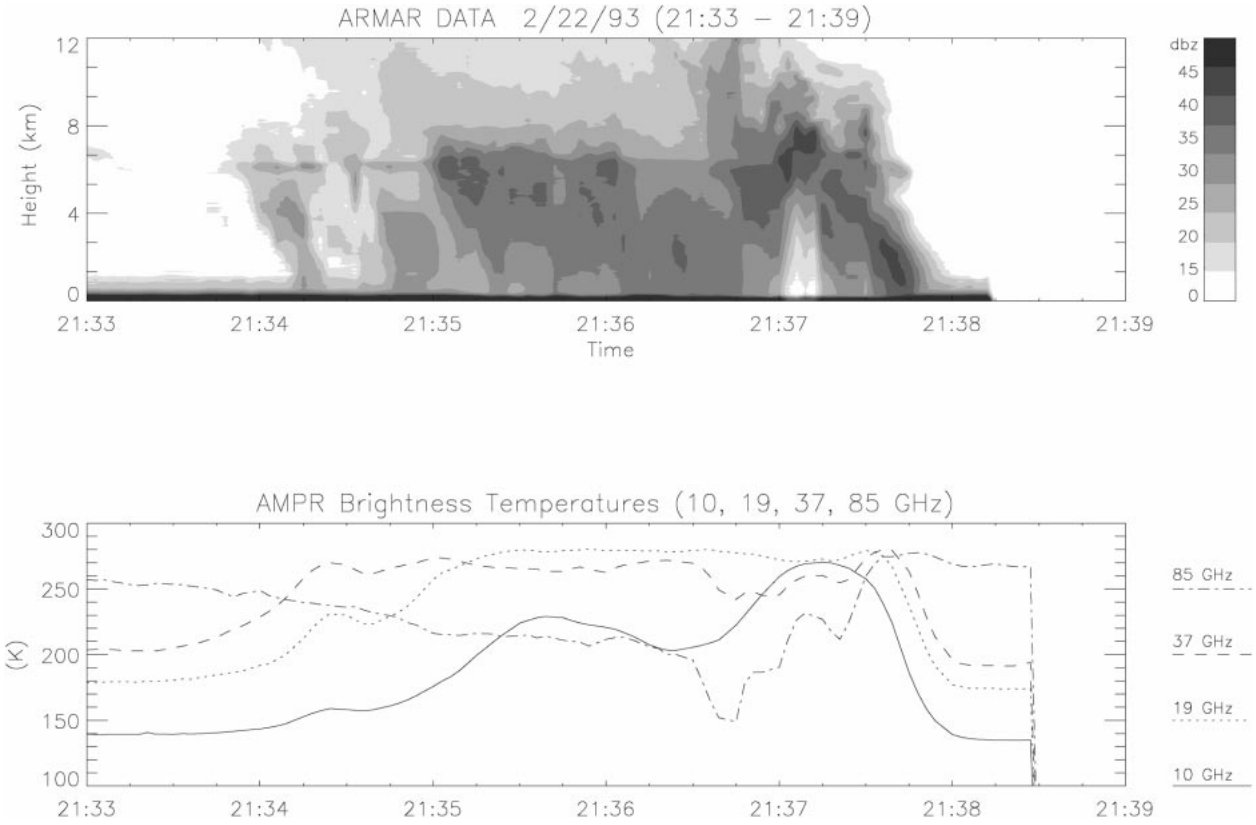


FIG. 1. A tilted convective system observed during TOGA COARE. (top) Radar reflectivities from ARMAR; (bottom) brightness temperatures from AMPR for 10, 19, 37, and 85 GHz.

ice, and the observed brightness temperature decreases over both ocean and land backgrounds. Rainfall retrieval from satellite passive microwave brightness temperatures has been investigated by many researchers (Wilheit et al. 1977; Spencer et al. 1989; Kummerow and Giglio 1994a,b; Smith et al. 1992).

Tropical precipitation generally occurs in the form of organized mesoscale convective systems (MCSs), which can be characterized by two distinguishable components: convective and stratiform regions (see Zipser 1977; Leary and Houze 1979; and Houze 1989 for detailed descriptions of MCSs). Convective regions range from a few kilometers to about 30 km in scale and have strong updrafts and downdrafts; in contrast, stratiform regions may extend for hundreds of kilometers and have relatively weak vertical air motion and light precipitation. Strong ice scattering associated with deep convection has been observed by passive microwave radiometers (Wilheit et al. 1982) because of the vigorous updrafts in convective regions. McGaughey et al. (1996) have found significant ice scattering in stratiform precipitation regions, however. In such cases, convective cores and rain shafts are tilted rearward as mesoscale systems propagate. Thus, the ice particles aloft shift horizontally away from heavy surface rainfall regions.

If a mesoscale system is tilted, 85-GHz brightness temperatures ($Tb_{85}$) that respond to cloud ice will be displaced from brightness temperature at 10 or 19 GHz ($Tb_{10}$ or $Tb_{19}$) that respond primarily to surface rainfall and liquid hydrometeors in lower layers of clouds. These tilted convective systems have been noted by Zipser (1977), Houze (1977), and LeMone et al. (1984). They also were observed by aircraft radar and radiometer as well as ground-based radar during the Tropical Ocean and Global Atmosphere Coupled Ocean–Atmosphere Response Experiment (TOGA COARE). Figure 1 depicts one case that was observed by the Airborne Rain-Mapping Radar (ARMAR) and the Advanced Microwave Precipitation Radiometer (AMPR).

Satellite passive microwave radiometers such as the Special Sensor Microwave Imager (SSM/I) (Hollinger et al. 1987) and the Tropical Rainfall Measurement Mission (TRMM) Microwave Imager (TMI) (Kummerow et al. 1998) observe the atmosphere at an oblique angle. Thus, the brightness temperatures associated with a tilted system viewed from one direction may be different than those observed from the opposite direction because of the different optical path. The displacement between $Tb_{85}$ and $Tb_{19}$ and the viewing angle–dependent brightness temperatures may result in errors of retrieved rainfall in a tilted system. Thus, investigation of microwave

brightness temperatures from tilted convective systems is important for improving satellite rainfall retrieval.

In this paper, brightness temperatures from tilted systems in different channels and at different viewing directions are investigated. Brightness temperatures are computed for a simple tilted cloud model and a cloud-resolving model. To account for the effect of tilt, the 3D backward Monte Carlo radiative transfer model developed by Roberti et al. (1994) is used and will be described in section 2. Brightness temperatures from tilted systems calculated using cloud/radiative models will be presented and discussed in section 3. The successful launch and operation of the TRMM satellite provides an opportunity to examine tilted convective systems using collocated radar and radiometer data. In section 4, satellite observations of tilted convective systems from the Precipitation Radar (PR), TMI, and SSM/I are presented. Conclusions and summary are given in section 5.

## 2. Radiative transfer model

Although 1D plane-parallel radiative transfer models are widely used in microwave spectral regions (Wilheit et al. 1977; Kummerow 1993), 3D radiative transfer models have been developed for horizontally and vertically finite clouds. Weinman and Davies (1978) first developed such a model but assumed vertical homogeneity. Kummerow and Weinman (1988) continued this study to include both liquid and ice layers and found that footprint-averaged brightness temperatures from finite clouds deviated considerably from the plane-parallel approximation. Haferman et al. (1993) used the discrete ordinates method to develop a 3D radiative transfer model and reported that the nadir brightness temperatures from a finite cloud over land were lower than the nadir brightness temperature from a horizontally infinite cloud because of net leakage of radiation through the sidewalls of the cloud. Both Petty (1994) and Roberti et al. (1994) developed a 3D backward Monte Carlo radiative transfer model and compared 1D versus 3D microwave radiative transfer calculations through an idealized cuboidal cloud model and a realistic cloud-resolving model, respectively.

The so-called 3D effect, which is the difference of brightness temperature over a finite cloud and a horizontally infinite cloud, can be attributed to geometric and physical problems (see Haferman et al. 1996). Geometrically, nonzero view angles lead to a larger brightness temperature pattern than rainfall pattern and a horizontal shift between brightness temperature field and surface rain field. Physically, radiation from the side walls of a finite cloud and the reflected image of cloud by the surface distorts the brightness temperature pattern from the surface rain field. These 3D effects also are reported by Liu et al. (1996) and Bauer et al. (1998).

To compute microwave brightness temperatures for a tilted system, a 3D radiative transfer model must be used to account for the effect of the tilt. In this paper, the 3D backward Monte Carlo radiative transfer model developed by Roberti et al. (1994) is used. The backward Monte Carlo method tracks photons that are received by airborne or satellite-borne radiometers back to their sources through the medium, following probabilistic interaction laws that are sampled by the selection of numbers from a quasi-random sequence. The photons are either absorbed or scattered at an interaction point. If a photon is absorbed, it is considered to be emitted at the temperature of the point of absorption. When a photon is scattered, a new direction of travel is determined by the phase function, which is assumed to be a Henyey–Greenstein phase function having a given asymmetry factor. If a photon collides with the surface, scattering or absorption occurs, depending on the surface emissivity and a randomly generated number. If a photon escapes from the upper boundary of the cloud, then it is considered to be emitted at the cosmic background temperature of 2.7 K.

Emission and absorption due to atmospheric gases (water vapor and oxygen) and hydrometeors, multiple scattering by hydrometeors, surface emission, and cosmic background radiation all are included in this model. A more detailed description of the 3D backward Monte Carlo model can be found in Roberti et al. (1994). The extinction and absorption coefficients of atmospheric gases (water vapor and oxygen) are computed using the formulas of Ulaby et al. (1981). Both liquid and ice are assumed to follow Marshall–Palmer drop size distributions. Radiative properties of atmospheric hydrometeors are computed using Mie theory.

## 3. Microwave brightness temperatures from tilted clouds

To examine the microwave brightness temperatures from tilted systems, the 3D backward Monte Carlo radiative transfer model is applied to two clouds. One is a simple finite cloud and the other is simulated using the Goddard Cumulus Ensemble (GCE) model, which is a cloud microphysical model developed primarily by Tao and Simpson (1993). Brightness temperatures at 19 and 85 GHz in the horizontal polarization are computed at different viewing angles. For convenience, they will be referred to as $Tb_{19}$ and $Tb_{85}$. Results and discussion are given in this section.

### *a. Simple tilted cloud model*

Haferman et al. (1996) developed the simple finite cloud model depicted in Fig. 2a, in which a 51 km $\times$ 51 km $\times$ 0.5 km nonprecipitating cloud is centered over a 5 km $\times$ 5 km $\times$ 4.5 km rain shaft, and a 5 km $\times$ 5 km $\times$ 5 km ice layer is centered over the cloud layer. A 5 km $\times$ 5 km cloud core area is chosen because TMI has approximately 5-km resolution at 85 GHz. After Wilheit et al. (1977), it is assumed that the relative hu-

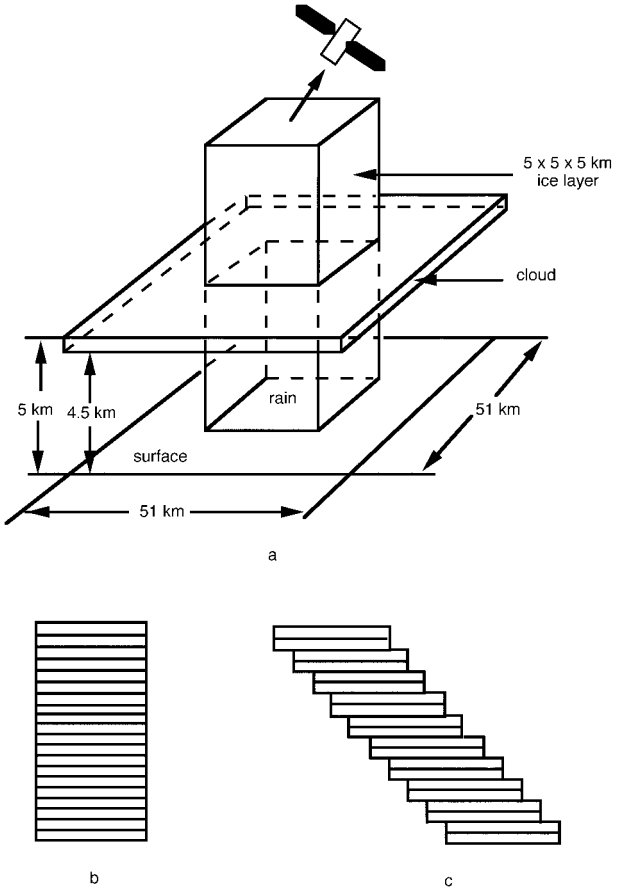


FIG. 2. A simple tilted cloud model. (a) Overview of vertical system; (b) sideview of the vertical rain shaft; and (c) sideview of tilted rain shaft.

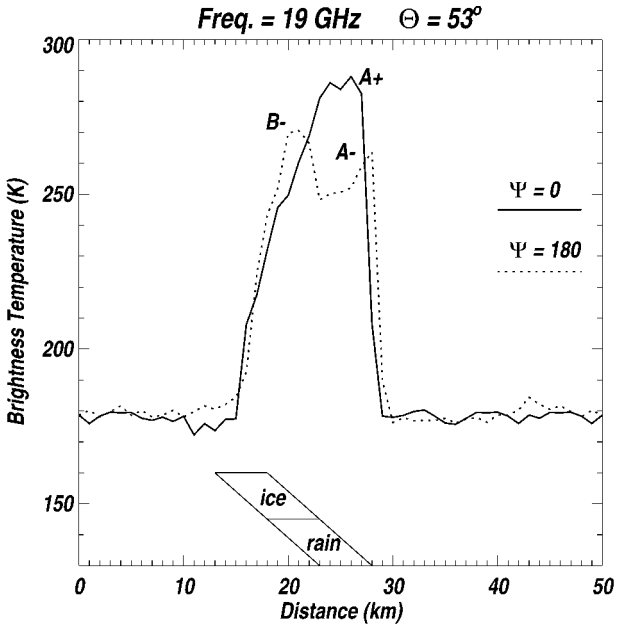


FIG. 3. 19-GHz brightness temperature of the simple tilted cloud model at the azimuth angles of 0° (solid line, looking from top right to bottom left) and 180° (dash line, looking from top left to bottom right). The tilted rain and ice shafts are laid over the plot. Letters A and B represent for the right and left sides of the cloud model, respectively. Subscripts "+" and "−" to A and B correspond to the view directions $\psi = 0°$ and $\psi = 180°$, respectively. Incident angle $= \Theta$.

midity in the model increases linearly from 80% at the surface to 100% at the freezing level (5 km). The temperature of the atmosphere increases from 273 K at the freezing level to 305 K at surface with a lapse rate of 6.5 K km$^{-1}$, and the wind speed at the surface is set to 0 m s$^{-1}$. A liquid water content of 0.5 g m$^{-3}$ is assumed for the nonprecipitating cloud extending 0.5 km below the freezing level. The density of ice is assumed to be 0.92 g cm$^{-3}$. Marshall–Palmer drop size distributions are assumed for both liquid and ice. To account for the effect of tilt, this model was modified by assuming that the central rain and ice shafts are tilted 45° toward the $\psi = 180°$ direction (to the left in Fig. 2). Figures 2b,c display side views of the vertical and tilted systems.

The 3D backward Monte Carlo radiative transfer model is applied to the tilted cloud systems. Brightness temperatures at 19 and 85 GHz at an incident angle of 53° are computed for a rain rate of 20 mm h$^{-1}$. Presented in Fig. 3 are the 19-GHz brightness temperatures at azimuth angles of 0° (solid line, looking from top right to bottom left) and 180° (dashed line, looking from top left to bottom right). It can be seen that the brightness temperature pattern is larger than the surface rain field. This result is due to the tilt that results in an increase of the radiated area viewed by satellite, and also is because radiation leaked from the side of the rain shaft. To understand these 3D effects better, the tilted rain and ice column is overlaid on Fig. 3. Letters A and B represent the right and left sides of the model, respectively. Subscripts "+" and "−" to A and B correspond to the view directions $\psi = 0°$ and $\psi = 180°$, respectively.

The major difference in the 19-GHz brightness temperatures when the tilted system is viewed from right and left ($\psi = 0°$ and 180°) is that the Tb for $\psi = 180°$ is less than the Tb for $\psi = 0°$. This difference results from the different radiative transfer paths, one of which passes through the entire cloud ice layer ($\psi = 180°$), but the other does not ($\psi = 0°$). The ice scattering creates a difference of more than 20 K between the two viewing directions (see $A_-$ and $A_+$ in Fig. 3).

Figure 4 shows the brightness temperatures of the tilted cloud for 85 GHz. The tilted rain and ice column have been laid over the figure. Unlike the 19-GHz channel that responds to liquid hydrometers at lower layers in the cloud, the 85-GHz channel responds primarily to the ice in upper layers of a cloud. Thus, the geometric shift, mentioned in Haferman et al. (1996), will cause the low $Tb_{85}$ to be displaced from the surface rainfall field. The tilt, however, results in the low $Tb_{85}$ being shifted farther from the surface rainfall field at $\psi = 0°$ (see $B_+$ in Fig. 4), and the low $Tb_{85}$ is closer to the

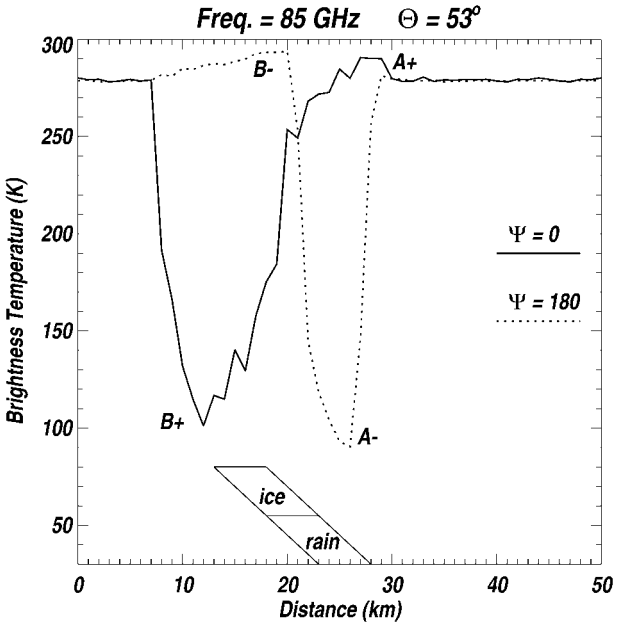


FIG. 4. Same as Fig. 3 but for 85 GHz.

surface rainfall field at $\psi = 180°$ (see $A_-$ in Fig. 4). The depression of 85-GHz brightness temperatures at the azimuth angle of 0° has a larger pattern than that of brightness temperatures at the azimuth angle of 180° because of the tilt of the ice layer. Besides depression, the $Tb_{85}$ is warmer than the background in the viewing direction (see $A_+$ and $B_-$ in Fig. 4). This feature, resulting from the ''reflected image,'' has been identified by both W. Olson in previous work and Petty (1994). It can be explained by the fact that the emission from liquid water at lower layers is reflected by the surface. This phenomenon exists in all 85-GHz images shown later.

Results from the simple tilted cloud model indicate sensitivity of brightness temperature to azimuthal view angle. At 19 GHz, the difference could be more than 20 K if ice is present when the surface rain field is viewed from the direction of tilt ($\psi = 180°$; see Tb at $A_-$ in Fig. 3) and viewed from the direction away from tilt ($\psi = 0°$; see Tb at $A_+$ in Fig. 3). For 85 GHz, the depressed brightness temperatures are shifted farther from surface rainfall regions at $\psi = 0°$. Variances of Tb85 viewed from both directions depend on thickness and slope of the ice layer. The higher $Tb_{85}$ from the reflected image is located on different sides of the cloud depending on azimuthal viewing angles.

### *b. GCE cloud model*

In section 3a, a simple tilted cloud model was tested. To understand better the effect of tilt, a more-realistic dynamical cloud model, the GCE, is used in this section. In the model, it is assumed that liquid and ice precipitating particles are spherical. The size distributions of rain, snow, and graupel (or hail) are taken to be inversely exponential with respect to the diameter $D$ such that

$$N(D) = N_0 \exp(-\lambda D),$$

where $N(D)$ is the number of drops of diameters between $D$ and $D + dD$ per unit volume, $N_0$ is the intercept parameter, and $\lambda$ is the slope of the distribution given by

$$\lambda = \left(\frac{\pi \rho_x N_0}{\rho q_x}\right)^{0.25},$$

where $\rho$ is the density of moist air, and $\rho_x$ and $q_x$ are the density and mixing ratio for hydrometeors, respectively.

The typical intercept parameters used in the GCE model for rain, snow, and graupel are 0.08 $cm^{-4}$, 0.04 $cm^{-4}$, and 0.04 $cm^{-4}$, respectively. The densities of rain, snow, and graupel are 1 g $cm^{-3}$, 0.1 g $cm^{-3}$, and 0.4 g $cm^{-3}$, respectively. Cloud ice is monodisperse with a diameter of $2 \times 10^{-3}$ cm and a density of 0.917 g $cm^{-3}$.

A 6-h GCE tropical squall line simulation is sampled at 60-min intervals from 60 min to 360 min. The model domain is a $128 \times 128 \times 28$ grid with a horizontal resolution of 3 km and vertical resolutions of 0.5 km in the lower 20 layers and 1 km in the upper eight layers. The tropical squall line was initialized using an environment observed on 22 February 1993 during TOGA COARE. Readers are referred to Tao and Simpson (1993) for additional details. The integrated precipitating liquid and ice from the GCE model at the simulation time of 240 min are shown in Fig. 5a. Figure 5b shows the vertical profile of precipitating liquid and ice along the transect CC′. It can be seen that the squall line is upshear tilted.

The Monte Carlo radiative transfer model is applied to examine brightness temperatures from the model clouds. Figures 6a,b present brightness temperatures at 19 GHz at azimuth angles of 0° and 180°, respectively. One can see the apparent brightness temperature difference of the squall line at 19 GHz when viewed from the front ($\psi = 0°$) and from the rear ($\psi = 180°$). At $\psi = 0°$, the strong emission near the leading edge of the squall line is a combination of radiation directly from heavy rain and radiation from rain reflected by the surface (see Fig. 6a), and, at $\psi = 180°$, the emission from the leading edge has been attenuated by passing back through the ice layers in the cloud system (see Fig. 6b). Brightness temperatures for 85 GHz at azimuth angles of 0° and 180° are displayed in Figs. 6c,d, respectively. Brightness temperatures that exceed the background values can be seen clearly along the boundary of the raining region in the viewing directions.

Brightness temperatures along the transect CC′ in Fig. 5a are displayed in Figs. 7 and 8. Figures 7a,b compare brightness temperatures at two azimuth angles at 19 GHz and 85 GHz, respectively. We can see from Fig. 7a that different optical paths result in lower brightness temperatures for $\psi = 180°$. Because of radiation leaked

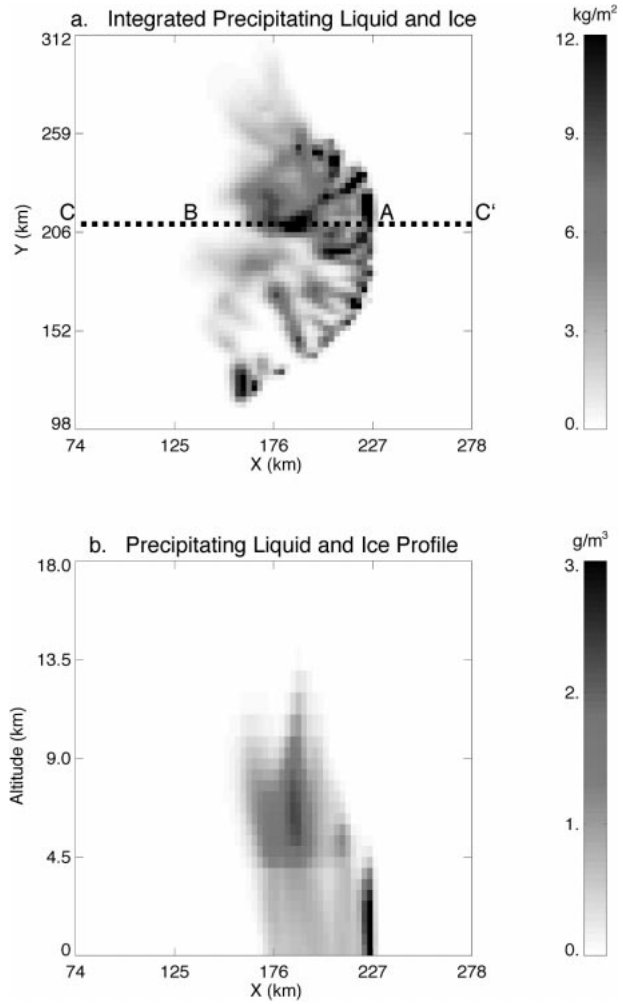


FIG. 5. The TOGA COARE GCE cloud model at the simulation time of 240 min. (a) Integrated precipitating liquid and ice; (b) vertical profile of the precipitating liquid and ice at the transect CC′.

from the side of the rain, brightness temperatures along the rain boundary always are higher at the viewing side than those viewed from the other side. Figure 7b shows that the locations for the strongest scattering of $Tb_{85}$ at $\psi = 0°$ and $\psi = 180°$ differ by about 10 km (see $B_+$ and $B_-$). This difference results from the geometric shift in 3D radiative transfer computation that was mentioned earlier. Emission from the reflected images can be seen clearly in the viewing directions (see $A_+$ and $A_-$ in Fig. 7b).

Figures 8a,b compare 19-GHz and 85-GHz brightness temperatures at $\psi = 0°$ and $\psi = 180°$, respectively. As discussed previously, the 3D radiative transfer model gives the brightness temperature at the top of the atmosphere. Therefore, as long as there is a nonzero viewing angle, $Tb_{19}$ actually responds to hydrometeors at different vertical levels than $Tb_{85}$ does. In other words, even in a vertically finite cloud system with liquid water in the lower cloud and ice in the upper cloud, 3D computations of high $Tb_{19}$ due to emission and low $Tb_{85}$ due to scattering from the same vertical profile will be dislocated. The degree of dislocation depends on the thickness of rain and ice layers. This dependence makes quantitative examination of displacement between $Tb_{19}$ and $Tb_{85}$ due to the tilt extremely difficult. One thing we can conclude is that the tilt of rain and ice shafts may result in a larger displacement between 19- and 85-GHz precipitation signatures. The scattering features are seen also for 19-GHz data, especially for $\psi = 180°$ (see Fig. 8b).

### c. *Different satellite field of view (FOV)*

Sections 3a,b give brightness temperatures at the resolutions of cloud models. What we are interested in, however, is how brightness temperatures change in a satellite FOV. In this section, SSM/I and TMI data are considered.

SSM/I has seven channels: 19.35 vertical (V) and horizontal (H) polarizations, 22.235 V, 37 V and H, and 85.5 V and H GHz. TMI also has the 19.35, 37, and 85.5 V and H channel pairs, plus two 10.7-GHz channels (V and H), and a 21.3-GHz water vapor absorption channel instead of the 22.235-GHz channel to avoid saturation in the Tropics. TMI footprint dimensions range from about 40 km for the 10-GHz channels to 5 km for the 85.5-GHz channels. SSM/I has horizontal resolutions from about 48 km for the 19.35-GHz channels to 13 km for the 85.5-GHz channels. Table 1 lists characteristics of TMI and SSM/I.

The simulated brightness temperatures in a satellite FOV are computed by convolving the high-resolution brightness temperature field with the antenna gain function. The antenna gain function has been discussed and used by Kummerow et al. (1996) and Olson et al. (1996). Figures 9a,b display the 19-GHz brightness temperature from the GCE model at the TMI resolution (~20 km) for $\psi = 0°$ and $\psi = 180°$, respectively. Comparing Figs. 9a,b with Figs. 6a,b, one can see that the low-resolution TMI data have smoothed features, such as the leading edge of the squall line, in comparison with the high-resolution images. For the SSM/I resolution, which is presented in Figs. 9c,d, the leading edge of the squall line is barely apparent when viewed from the rear of the system. Although the strong emission in the leading edge of the squall line still is visible at both TMI and SSM/I resolutions when viewed from the front ($\psi = 0°$), the difference of brightness temperature across the segment CC′ for azimuth angles of 0° and 180° is very small (see Fig. 11a and Fig. 13a).

Figures 10a–d present $Tb_{85}$ from the GCE model at TMI and SSM/I resolutions for $\psi = 0°$ and $\psi = 180°$, respectively. Because the 85-GHz brightness temperature for TMI has a resolution of 5 km, it almost retains the features at the GCE model's resolution (see Figs. 10a,b). Although $Tb_{85}$ from SSM/I shows the smoothed GCE model features, the brightness temperatures above

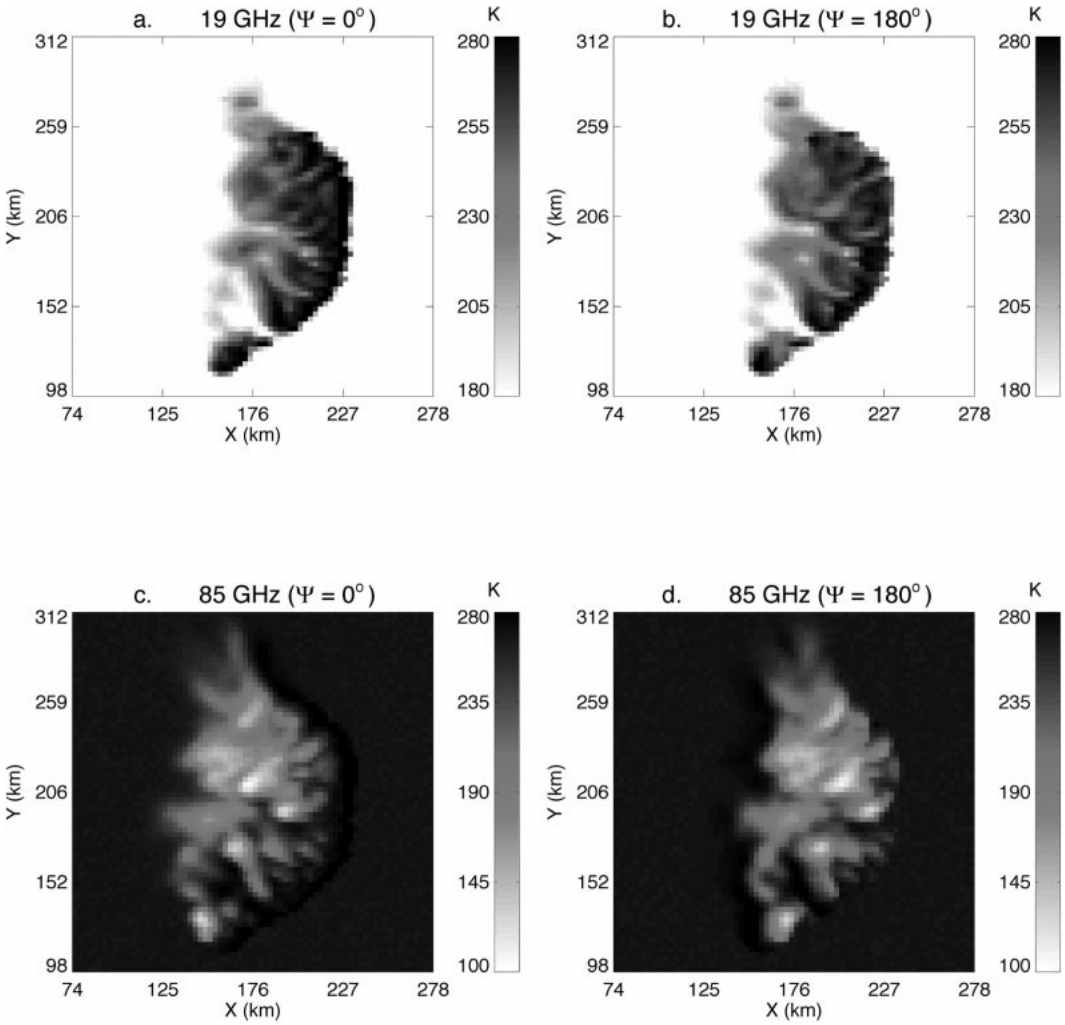


FIG. 6. Brightness temperatures from the GCE cloud model. (a) For 19 GHz, azimuth angle = 0° (looking from right side to left); (b) 19 GHz, azimuth angle = 180° (looking from left side to right); (c) 85 GHz, azimuth angle = 0°; and (d) 85 GHz, azimuth angle = 180°.

the background values due to emission from the side of the rain are clearly displayed in Figs. 10c,d. Figures 11b and 13b present the $Tb_{85}$ difference across the transect CC′ for azimuth angles of 0° and 180° at TMI and SSM/I resolutions, respectively. Figure 13b indicates that the $Tb_{85}$ difference between azimuth angles of 0° and 180° for the SSM/I is small.

Figures 12a,b present the displacement between $Tb_{19}$ and $Tb_{85}$ of TMI for azimuth angles of 0° and 180°, respectively. Figures 14a,b are the same as Figs. 12a,b but are for SSM/I. Note that the dislocation between high $Tb_{19}$ due to emission and low $Tb_{85}$ due to scattering is reduced as the resolution degrades.

The 3D radiative transfer computation results for $Tb_{19}$ and $Tb_{85}$ indicate that the brightness temperature from a tilted system varies when viewed from two opposite directions of the tilt. The $Tb_{85}$ will be displaced from $Tb_{19}$ if a mesoscale system is tilted. As the resolution degrades to satellite FOV, the difference of brightness temperatures viewed from two opposite directions of the tilt may be neglected. The displacement between $Tb_{19}$ and $Tb_{85}$ signatures, however, depends on the slope of a tilted convective system and the viewing direction. In other words, the displacement between $Tb_{19}$ and $Tb_{85}$ resulting from 3D physical and geometric effects may be neglected for low resolutions of satellite data, but if ice particles in a tilted convective system shift more than several satellite footprints from the surface rainfall field, the displacement between $Tb_{19}$ and $Tb_{85}$ cannot be ignored (see next section). This fact poses a problem for those rain retrieval algorithms that use only scattering information.

## 4. Satellite microwave observations of tilted systems

Satellite observations of tilted convective systems have been noticed by some researchers. Using ground-

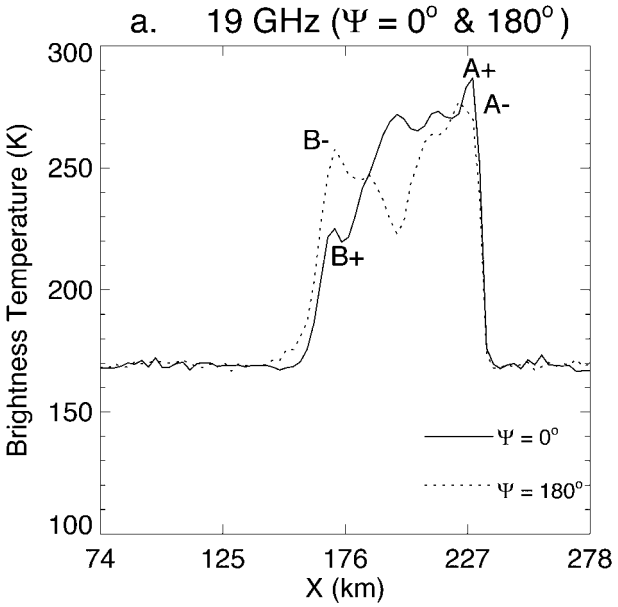


FIG. 7. Comparison of brightness temperatures along the cross line of CC′ at different azimuth angles. (a) For 19 GHz for azimuth angle = 0° (solid line) and azimuth angle = 180° (dash line); (b) 85 GHz for azimuth angle = 0° (solid line) and azimuth angle = 180° (dash line).

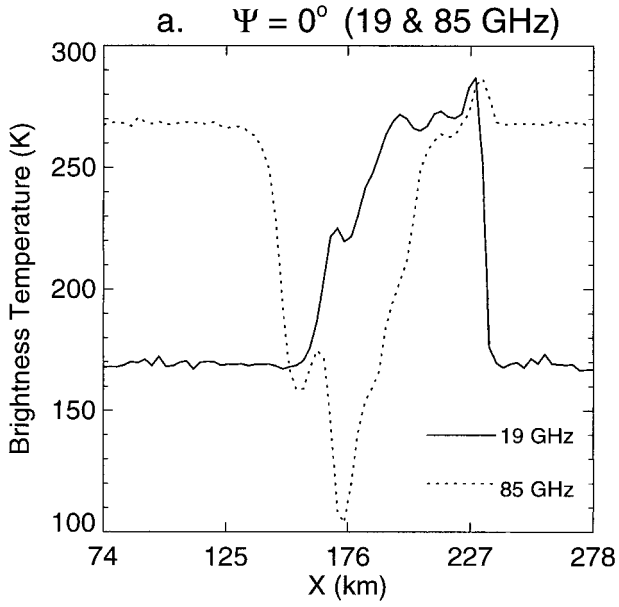


FIG. 8. Comparison of brightness temperatures along the cross line of CC′ at different channels. (a) Azimuth angle = 0° for 19 GHz (solid line) and 85 GHz (dash line); (b) azimuth angle = 180° for 19 GHz (solid line) and 85 GHz (dash line).

based radar data and infrared data from geostationary satellites, Zipser (1988) and Heymsfield and Fulton (1994) found that, in propagating squall line systems, the coldest cloud tops dislocated from the leading edge to the extensive trailing anvil as the systems evolve. Such characteristics also were found during TOGA COARE (Rickenbach et al. 1997). Those observations were limited to locations for which there were ground-based radars or aircraft field experiments. The success of the TRMM project has provided an opportunity to examine the tilted systems globally and frequently, because TRMM carries both the high-resolution microwave imager, TMI, and the first spaceborne PR. The PR is a cross-scanning 13.8-GHz radar that has a swath width of about 220 km, about one-third of TMI swath width. It can provide the 3D distribution of rainfall intensity at a horizontal resolution of about 4.4 km and a vertical resolution of about 250 m. The vertical rainfall profile from PR data can be used to detect the tilted

TABLE 1. Characteristics of TMI and SSM/I.

| Instrument | Frequency (GHz) | Spatial resolution (km) | Polarization (H, V) |
|---|---|---|---|
| SSM/I | 19.35 | 69 × 43 | H, V |
| | 22.235 | 50 × 40 | V |
| | 37 | 37 × 29 | H, V |
| | 85.5 | 15 × 13 | H, V |
| TMI | 10.7 | 63 × 37 | H, V |
| | 19.35 | 30 × 18 | H, V |
| | 21.3 | 23 × 18 | V |
| | 37 | 16 × 9 | H, V |
| | 85.5 | 7 × 5 | H, V |

system. TMI observations of tilted systems at 19 GHz and 85 GHz are examined in this section. For comparison, collocated and coincident SSM/I observations also are presented.

At the time of writing, the SSM/I data could be obtained from the Global Hydrology Resource Center at National Aeronautics and Space Administration (NASA) Marshall Space Flight Center (http://ghrc.msfc.nasa.gov) and TRMM data were available from the Distributed Active Archive Center at NASA Goddard Space Flight Center (http://daac.gsfc.nasa.gov).

### *a. Case of 5 January 1998*

A convective system around 0330 UTC on 5 January 1998 is depicted in Fig. 15. Figure 15a displays the near-surface PR reflectivity and Fig. 15b shows the cross section of reflectivity along line AA′. Three types of radar returns can be seen in Fig. 15b: 1) the backscatter return from hydrometeors, 2) the surface echo, and 3) the mirror-image return that corresponds to multiple scattering of the radar pulse between the surface and hydrometeors (Meneghini and Nakamura 1988; Liao et al. 1999).

It also can be seen from Fig. 15b that the maximum

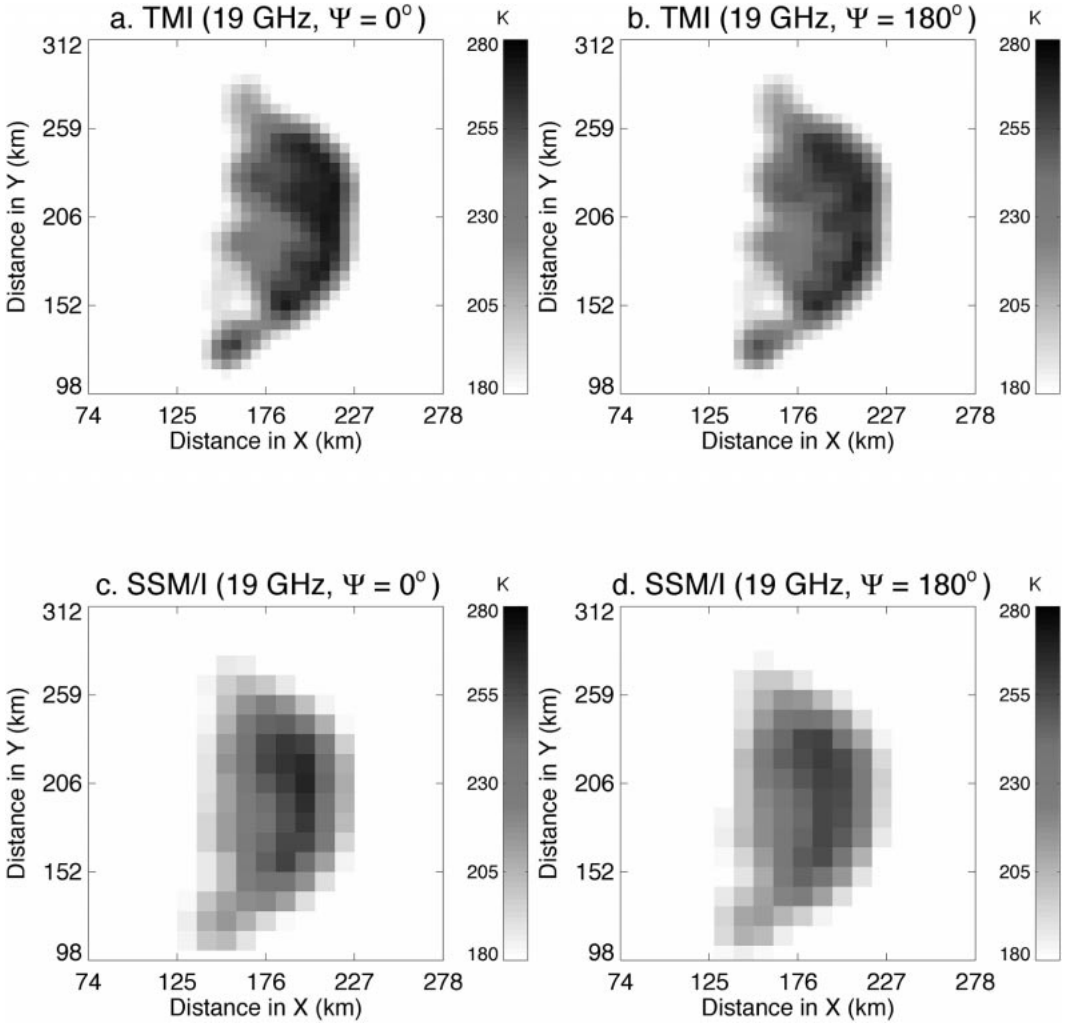


FIG. 9. The 19-GHz brightness temperatures of the GCE model at satellite radiometer resolution. (a) TMI, azimuth angle = 0°; (b) TMI, azimuth angle = 180°; (c) SSM/I, azimuth angle = 0°; and (d) SSM/I, azimuth angle = 180°.

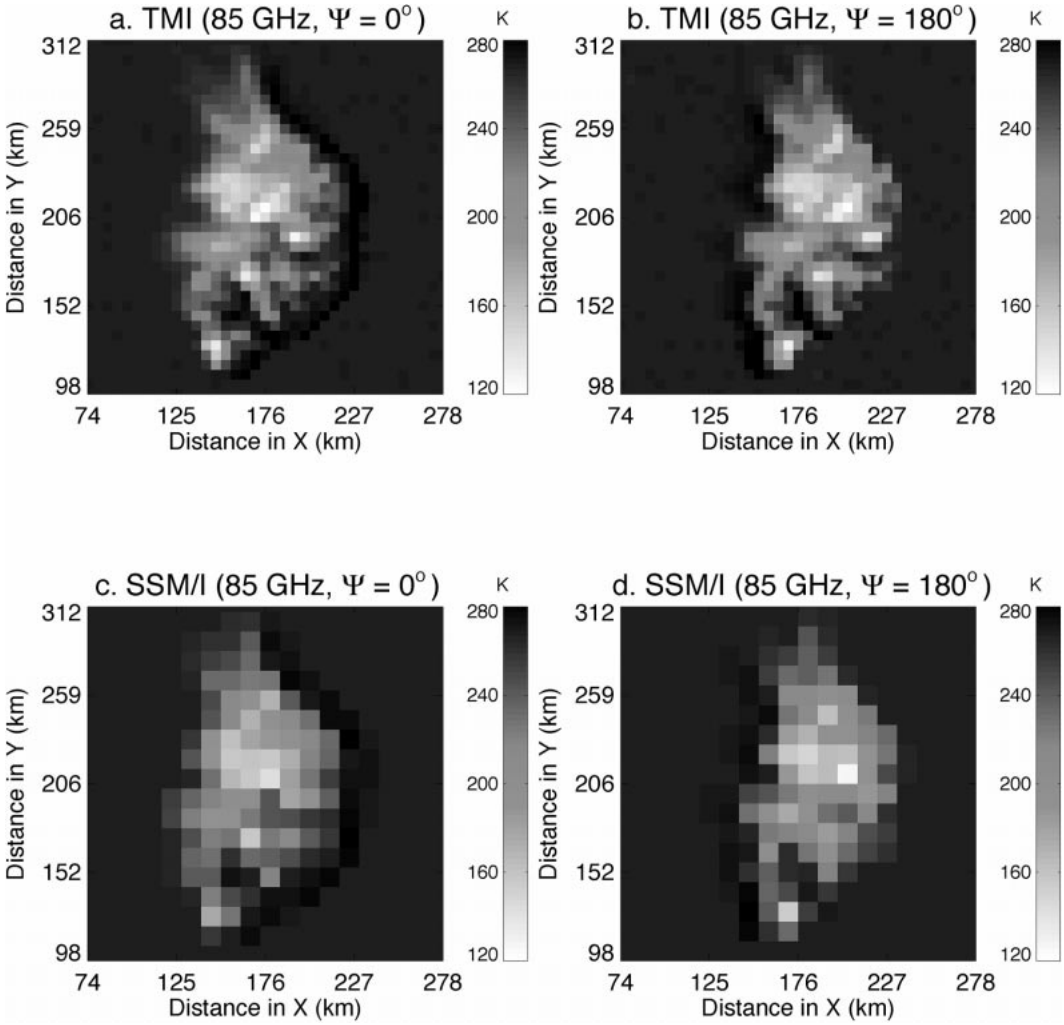


FIG. 10. Same as Fig. 9 but for 85 GHz.

surface rainfall occurs near 30°S and 132.5°W, and a large part of the ice particles aloft occur over the region west of 133°W. Existence of a bright band from 133° to 133.75°W suggests that the rainfall is stratiform in nature in this region. Thus, ice particles do not locate above the convective region but in the stratiform region. Some were even in the precipitation-free region.

Brightness temperatures for 19 and 85 GHz (horizontal polarization) from TMI are presented in Figs. 16a,b respectively. Note that the warm $Tb_{19}$ in Fig. 16b corresponds to the high surface reflectivity shown in Fig. 16a. Figure 16c shows $Tb_{19}$ and $Tb_{85}$ along the cross line AA′. Notice that the lowest $Tb_{85}$ along AA′, which responds to the strongest ice scattering, is about 1° (~100 km) to the west away from the highest $Tb_{19}$.

Figures 17a–c are the same as those in Figs. 16a–c but are for SSM/I observation of the case. Although the brightness temperatures vary more smoothly because of the degradation of spatial resolution, the shift between the maximum $Tb_{19}$ and minimum $Tb_{85}$ still is apparent in Fig. 17c.

### b. *Case of 25 August 1998*

Figure 18 illustrates the case for Hurricane Bonnie around 1110 UTC on 25 August 1998. The near-surface PR reflectivity and the vertical cross section along line AA′ (from 29°N, 75°W to 32°N, 72°W) are shown on Figs. 18a,b, respectively. The mirror-image return can be seen clearly. A strong convective core appears near 29.75°N, 74.25°W, and PR data show apparent attenuation below a height of 3 km. A large amount of ice particles have moved into the region centered over 30.25°N, 73.75°W, however.

The brightness temperatures for the 19- and 85-GHz channels from both TMI and SSM/I are presented in Fig. 19 and Fig. 20, respectively. In comparison with Fig. 18, one can see that high-resolution PR data display

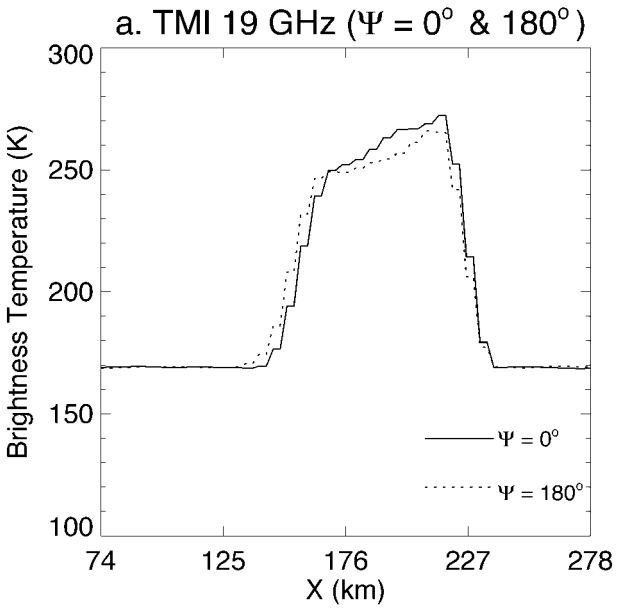


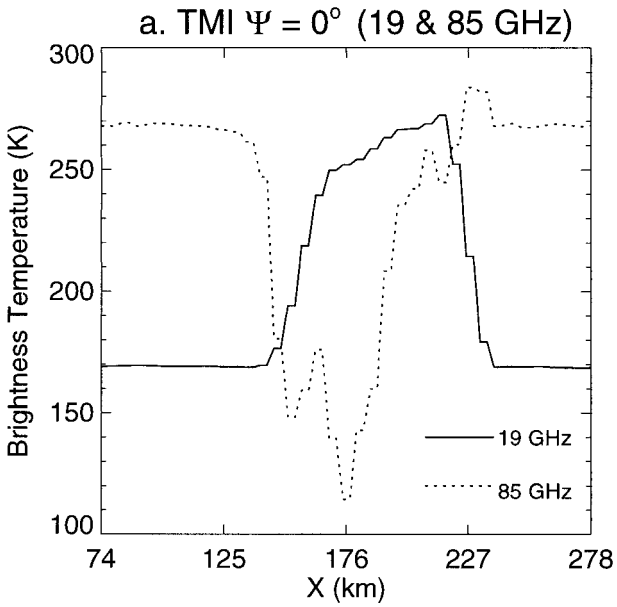


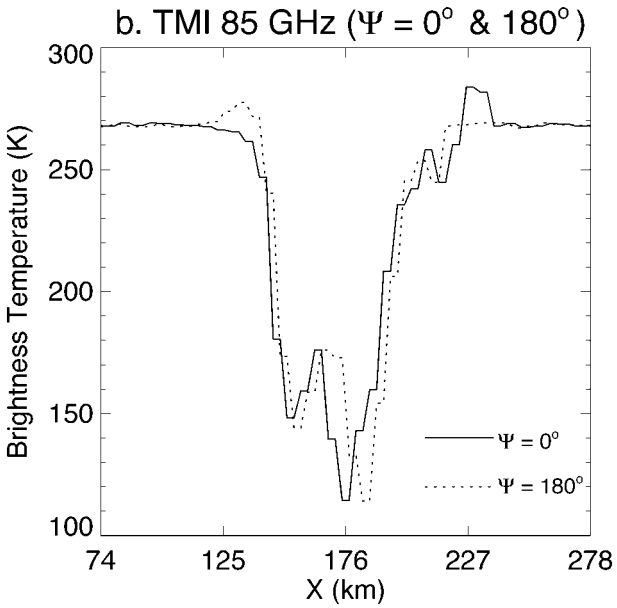


FIG. 11. Same as Fig. 7 but at TMI resolution.

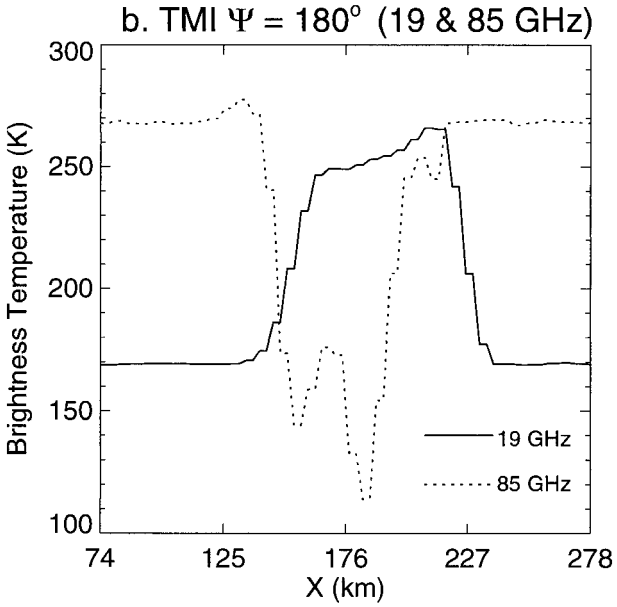


FIG. 12. Same as Fig. 8 but at TMI resolution.

a very narrow (about 10 km) rainfall band pattern, but TMI data cannot distinguish such a narrow band. Nevertheless, the displacements between 19-GHz and 85-GHz brightness temperatures along the line AA′ can be seen in both TMI (Fig. 19c) and SSM/I data (Fig. 20c). Note that, near longitude 74°W, the cold $Tb_{85}$ occur along latitude 30°N, and the warm $Tb_{19}$ appear along 29.75°N.

Passive microwave observations of the above-two cases confirm the results derived from model simulations and show that the dislocation between the heavy surface rainfall region and ice particles aloft can be as large as 100 km for TMI if a convective system is tilted. Satellite observations also indicate that, even for low-resolution SSM/I data, the displacement between $Tb_{19}$ and $Tb_{85}$ features can be appreciable. The displacement of low $Tb_{85}$ from surface rainfall is a potential problem for single-channel, 85-GHz surface rainfall retrieval algorithms and also potentially casts large retrieval uncertainty on multichannel retrieval algorithms. Such retrieval uncertainty has been found in the TRMM operational algorithm results for the above-two cases (not shown).

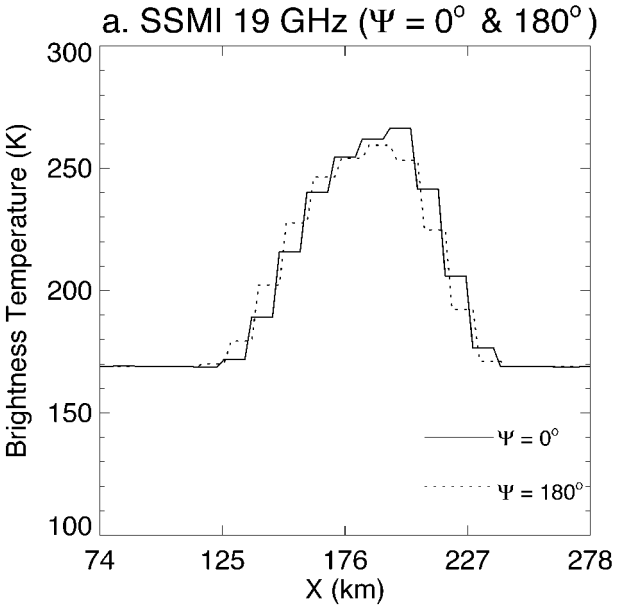


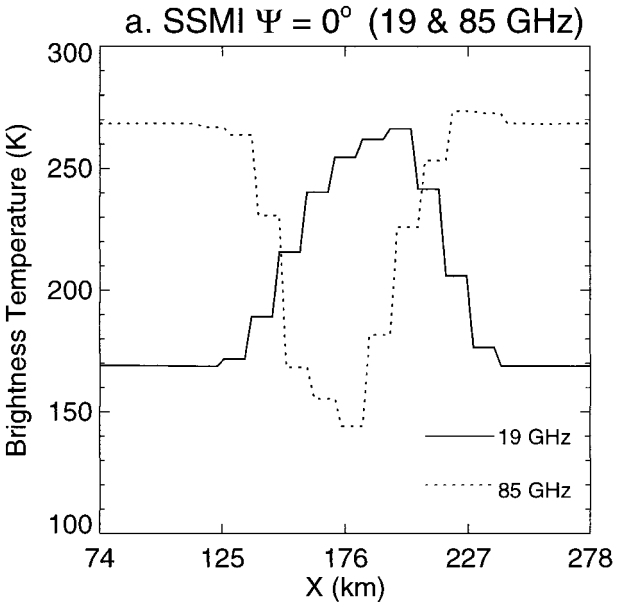


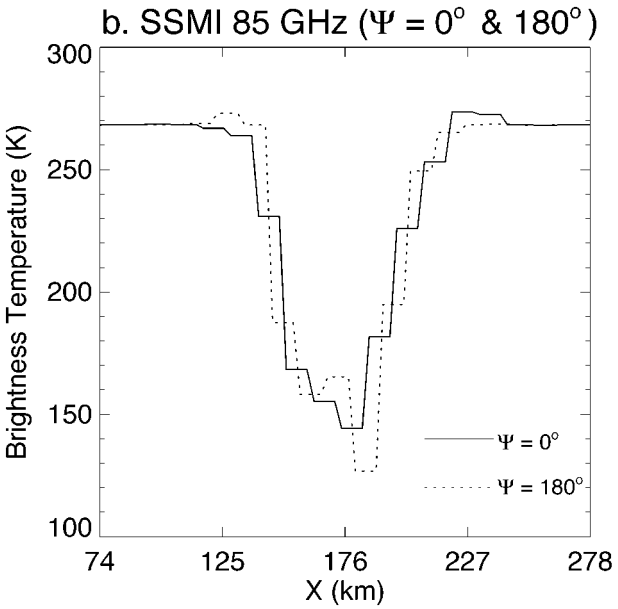


FIG. 13. Same as Fig. 7 but at SSM/I resolution.

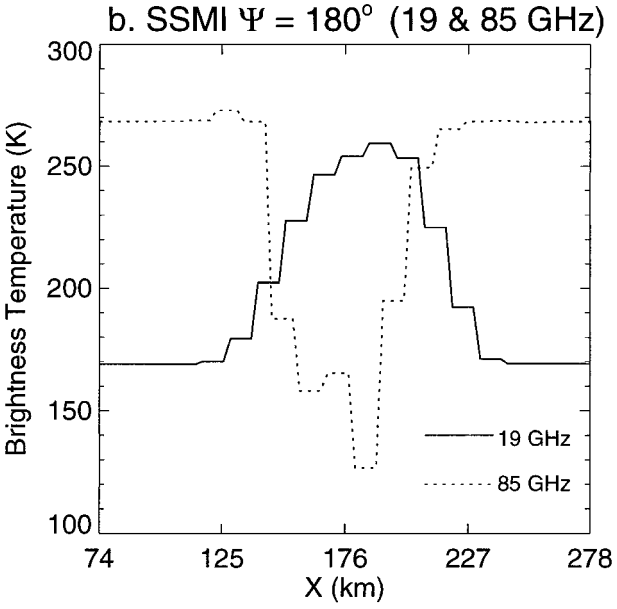


FIG. 14. Same as Fig. 8 but at SSM/I resolution.

## 5. Summary

Passive microwave brightness temperatures from tilted convective systems at 19 and 85 GHz have been examined using data computed from cloud models and measured from satellite radiometers. To account for the effect of tilt, a 3D backward Monte Carlo radiative transfer model has been applied to the simple tilted cloud model and to the GCE model to derive brightness temperatures. Results from the simple tilted cloud model indicate that brightness temperatures vary when azimuthal viewing angle changes. The difference of 19-GHz brightness temperatures over the surface rain field is caused by differing optical thickness from two opposite viewing directions. For 85 GHz, the depression of brightness temperatures may be shifted from the surface rainfall field depending on the tilt direction and the viewing direction. Variances of $Tb_{85}$ viewed from both directions rely on thickness and slope of the ice layer. The $Tb_{85}$ above the background values due to emission from the side of the cloud are located at different viewing directions.

Results from the GCE model show similar features. When viewed from the leading edge of a squall line, strong emission is apparent, caused by the radiation

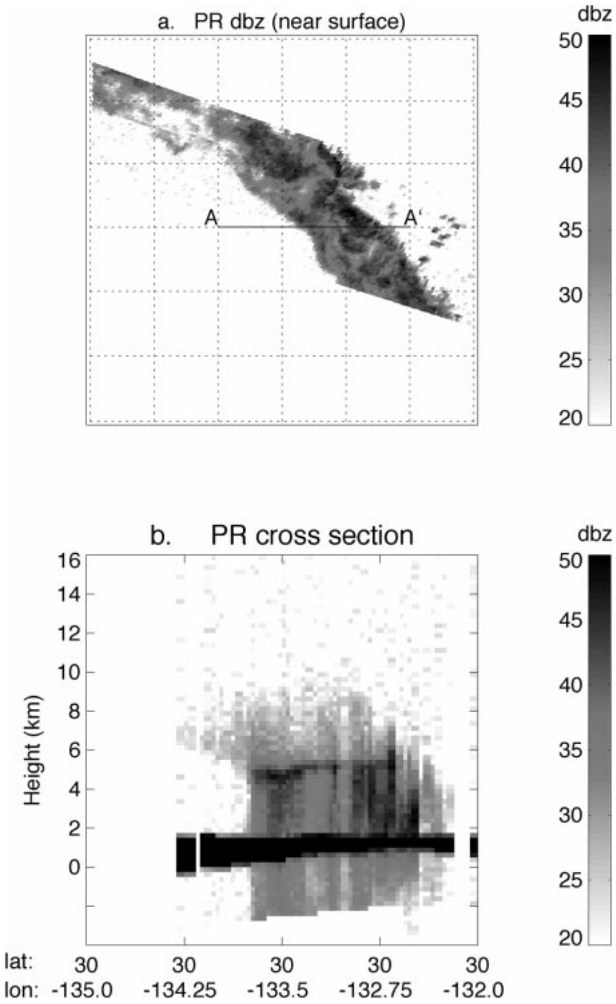


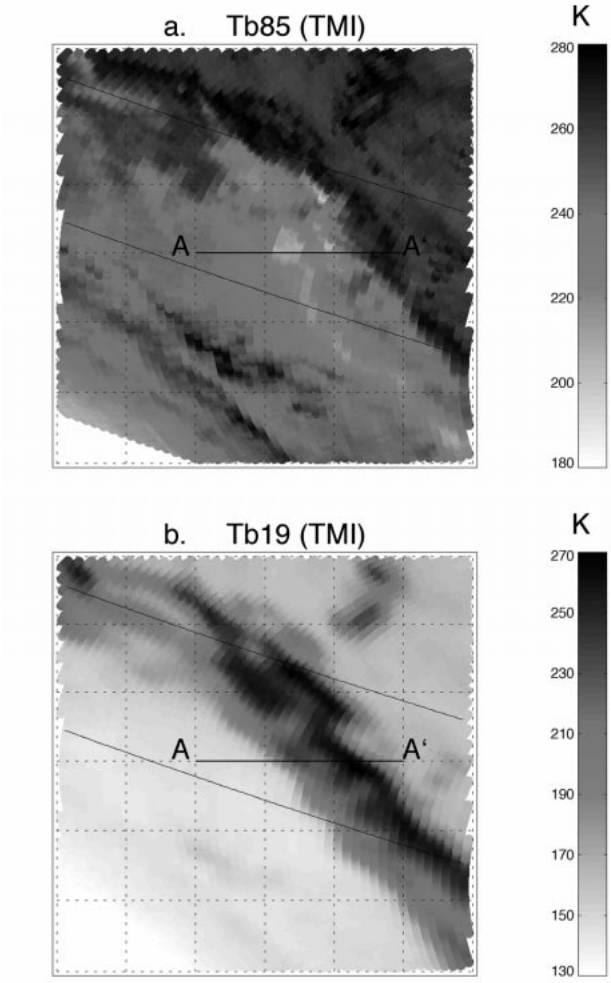


FIG. 15. Radar reflectivity from PR for a convective system around 0330 UTC on 5 Jan 1998. (a) Near-surface reflectivity; (b) cross section of reflectivity along line AA′.

leakage from the side of the rainfall region. Viewed from the rear, however, the emission from the heavy surface rainfall field is reflected by the ice on the top of the cloud so that $Tb_{19}$ is depressed. This study also confirms the finding by Petty (1994) that warm $Tb_{85}$, due to emission from the side of the cloud, exists along the cloud boundary at the viewing side. These phenomena cannot be reproduced using a plane-parallel radiative transfer model.

Because $Tb_{19}$ mostly responds to liquid hydrometeors in the low level of clouds and $Tb_{85}$ mainly responds to ice hydrometeor in the upper level of clouds, the 3D radiative transfer model–derived $Tb_{19}$ will be displaced from $Tb_{85}$ if there is an oblique viewing angle. This fact is true even for a vertical cloud system. But the displacement in vertical systems due to the 3D geometric and physical effects may be ignored for low-resolution satellite data. Results from section 3c suggest that such

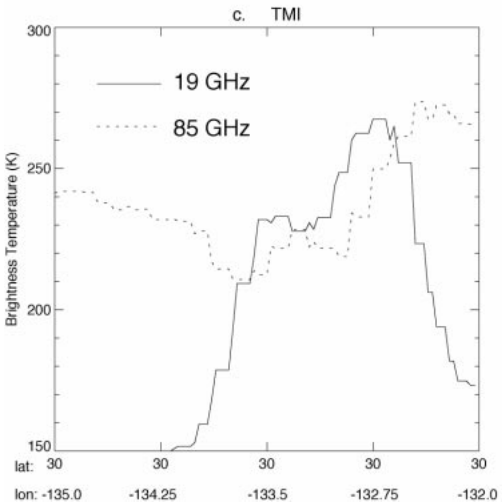


FIG. 16. TMI observations of the convective system around 0330 UTC on 5 Jan 1998. (a) For 85 GHz; (b) 19 GHz; and (c) $Tb_{85}$ and $Tb_{19}$ along the cross line of AA′. Lines on (a) and (b) are edges of PR swath.

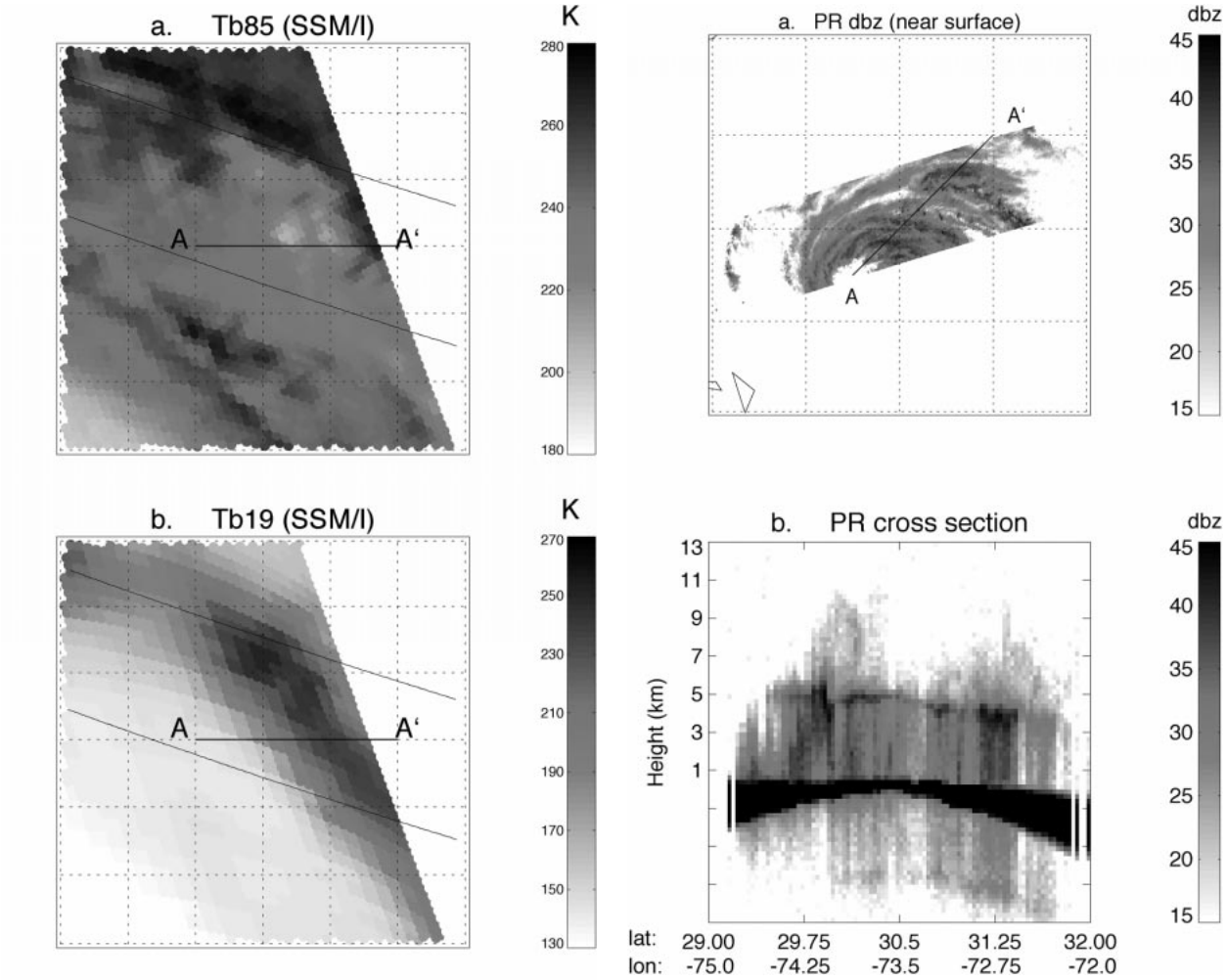


FIG. 18. Radar reflectivity from PR for the Hurricane Bonnie case around 1115 UTC on 25 Aug 1998. (a) Near-surface reflectivity; and (b) cross section of reflectivity along line AA′.

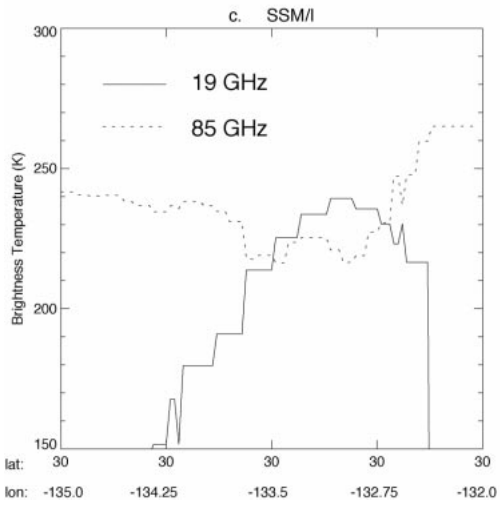


FIG. 17. Same as Fig. 16 but for SSM/I observations.

displacements are reduced dramatically as the resolution degrades.

The existence of tilt in convective systems, however, may increase such displacements depending on the slope of tilt and the viewing direction. Satellite observations of tilted systems indicate that dislocation between $Tb_{19}$ and $Tb_{85}$ cannot be neglected. The $Tb_{85}$ may be displaced from $Tb_{19}$ by as much 100 km. Such dislocation adds to uncertainty in rainfall retrieval.

The investigation of brightness temperatures from tilted systems suggests that care must be taken when scattering information from 85-GHz data is used as an indicator of surface rainfall or other index, such as separation of convective and stratiform regions (Anagnostou and Kummerow 1997; Hong et al. 1999). This is particularly true for the high-resolution TMI 85-GHz data. Using TMI data only, it may be difficult to detect the direction of tilt and remove the effect of tilt in surface rainfall retrieval. Combined with high-resolution

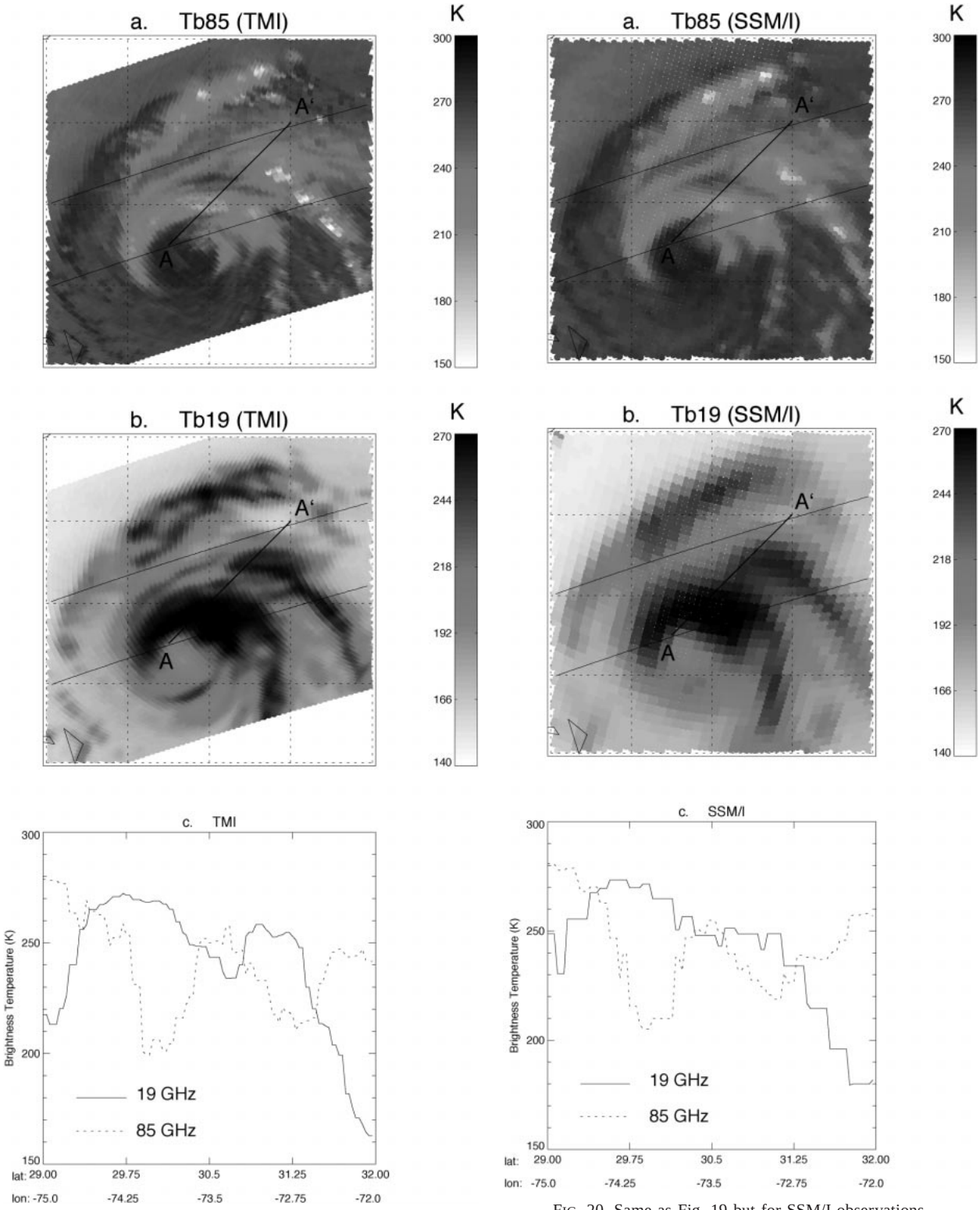


FIG. 19. TMI observations of the Hurricane Bonnie case around 1115 UTC on 25 Aug 1998. (a) For 85 GHz; (b) 19 GHz; and (c) $Tb_{85}$ and $Tb_{19}$ along the cross line of AA′.

FIG. 20. Same as Fig. 19 but for SSM/I observations.

PR data, however, the effect of tilt can be reduced, and the surface rainfall retrieval from satellite data will be improved.

*Acknowledgments.* We thank Drs. David Short and Tom Rickenbach for their helpful discussion and for providing the TOGA COARE radar data. We are grateful to Dr. Edward J. Zipser and two other anonymous reviewers for their constructive recommendations and comments. Thanks are due to Dr. Chris Kidd and Mr. Carlos Morales for their help on processing and displaying TRMM PR and TMI data. This work was funded by the TRMM science program.

## REFERENCES

Anagnostou, E. N., and C. Kummerow, 1997: Stratiform and convective classification of rainfall using SSM/I 85-GHz brightness temperature observations. *J. Atmos. Oceanic Technol.,* **14,** 570–575.

Bauer, P., L. Schanz, R. Bennartz, and P. Schlüssel, 1998: Outlook for combined TMI–VIRS algorithms for TRMM: Lessons from the PIP and AIP projects. *J. Atmos. Sci.,* **55,** 1714–1729.

Haferman, J. L., W. F. Krajewski, T. F. Smith, and A. Sanchez, 1993: Radiative transfer for a three-dimensional raining cloud. *Appl. Opt.,* **32,** 2795–2802.

——, E. N. Anagnostou, D. Tsintikidis, W. F. Krajewski, and T. F. Smith, 1996: Physically based satellite retrieval of precipitation using a 3D passive microwave radiative transfer model. *J. Atmos. Oceanic Technol.,* **13,** 832–850.

Heymsfield, G. M., and R. Fulton, 1994: Passive microwave and infrared structure of mesoscale convective systems. *Meteor. Atmos. Phys.,* **54,** 123–139.

Hollinger, J., R. Lo, and G. Poe, 1987: Special Sensor Microwave/Imager User's Guide. NRL Report, 177 pp. [Available from Space Sensing Branch, Naval Research Laboratory, 4555 Overlook Ave. SW, Washington, DC 20375.]

Houze, R. A., Jr., 1977: Structure and dynamics of a tropical squall-line system observed during GATE. Observed structure of mesoscale convective systems and implications for large-scale heating. *Mon. Wea. Rev.,* **105,** 1540–1567.

——, 1989: Observed structure of mesoscale convective systems and implications for large-scale heating. *Quart. J. Roy. Meteor. Soc.,* **115,** 425–461.

Kummerow, C., 1993: On the accuracy of the Eddington approximation for radiative transfer in the microwave frequencies. *J. Geophys. Res.,* **98,** 2757–2765.

——, and J. A. Weinman, 1988: Determining microwave brightness temperatures from precipitating horizontally finite and vertically structured clouds. *J. Geophys. Res.,* **93,** 3720–3728.

——, and L. Giglio, 1994a: A passive microwave technique for estimating rainfall and vertical structure information from space. Part I: Algorithm description. *J. Appl. Meteor.,* **33,** 3–18.

——, and ——, 1994b: A passive microwave technique for estimating rainfall and vertical structure information from space. Part II: Applications to SSM/I data. *J. Appl. Meteor.,* **33,** 19–33.

——, W. S. Olson, and L. Giglio, 1996: A simplified scheme for obtaining precipitation and vertical hydrometeor profiles from passive microwave sensors. *IEEE Trans. Geosci. Remote Sens.,* **34,** 1213–1232.

——, W. Barnes, T. Kozu, J. Shiue, and J. Simpson, 1998: The Tropical Rainfall Measuring Mission (TRMM) sensor package. *J. Atmos. Oceanic Technol.,* **15,** 809–817.

Leary, C. A., and R. A. Houze Jr., 1979: The structure and evolution of convection in a tropical cloud cluster. *J. Atmos. Sci.,* **36,** 437–457.

LeMone, M. A., G. M. Barnes, E. J. Szoke, and E. J. Zipser, 1984: The tilt of the leading edge of mesoscale tropical convective lines. *Mon. Wea. Rev.,* **112,** 510–519.

Liao, L., R. Meneghini, and T. Iguchi, 1999: Simulations of mirror image returns of air/space-borne radars in rain and their applications in estimating path attenuation. *IEEE Trans. Geosci. Remote Sens.,* **37,** 1107–1121.

Liu, Q., C. Simmer, and E. Ruprecht, 1996: Three-dimensional radiative transfer effects of clouds in the microwave spectral range. *J. Geophys. Res.,* **101,** 4289–4298.

McGaughey, G., E. J. Zipser, R. W. Spencer, and R. E. Hood, 1996: High-resolution passive microwave observations of convective systems over the tropical Pacific Ocean. *J. Appl. Meteor.,* **35,** 1921–1947.

Meneghini, R., and K. Nakamura, 1988: Some characteristics of the mirror-image return in rain. *Tropical Rainfall Measurements,* J. S. Theon and N. Fugono, Eds., Deepak Publishing, 235–242.

Olson, W. S., C. D. Kummerow, G. M. Heymsfield, and L. Giglio, 1996: A method for combined passive–active microwave retrievals of cloud and precipitation profiles. *J. Appl. Meteor.,* **35,** 1763–1789.

Petty, G. W., 1994: Physical retrievals of over-ocean rain rate from multichannel microwave imagery. Part I: Theoretical characteristics of normalized polarization and scattering indices. *Meteor. Atmos. Phys.,* **54,** 79–99.

Rickenbach, T. M., D. A. Short, and O. W. Thiele, 1997: Propagation characteristics of tropical convective systems from radar and infrared satellite images. Preprints, *28th Conf. on Radar Meteorology,* Austin, TX, Amer. Meteor. Soc., 596–597.

Roberti, L., J. L. Haferman, and C. Kummerow, 1994: Microwave radiative transfer through horizontally inhomogeneous precipitating clouds. *J. Geophys. Res.,* **99,** 16 707–16 718.

Smith, E. A., A. Mugnai, H. J. Cooper, G. J. Tripoli, and X. Xiang, 1992: Foundations for statistical physical precipitation retrieval from passive microwave satellite measurements. Part I: Brightness temperature properties of a time-dependent cloud radiation model. *J. Appl. Meteor.,* **31,** 506–531.

Spencer, R. W., H. M. Goodman, and R. E. Hood, 1989: Precipitation retrieval over land and ocean with the SSM/I: Identification and characteristics of the scattering signal. *J. Atmos. Oceanic Technol.,* **6,** 254–273.

Tao, W.-K., and J. Simpson, 1993: Goddard Cumulus Ensemble model, Part I: Model description. *Terr. Atmos. Oceanic Sci.,* **4,** 35–72.

Ulaby, F. T., R. K. Moore, and A. K. Fung, 1981: *Microwave Remote Sensing Fundamentals and Radiometry.* Vol. 1, *Microwave Remote Sensing: Active and Passive,* Artech House, 456 pp.

Weinman, J. A., and R. Davies, 1978: Thermal microwave radiances from horizontally finite clouds of hydrometeors. *J. Geophys. Res.,* **83,** 3099–3107.

Wilheit, T. T., A. T. C. Chang, M. S. V. Rao, E. B. Rodgers, and J. S. Theon, 1977: A satellite technique for quantitatively mapping rainfall rates over the oceans. *J. Appl. Meteor.,* **16,** 551–560.

——, and Coauthors, 1982: Microwave radiometric observations near 19.35, 92, and 183 GHz of precipitation in Tropical Storm Cora. *J. Appl. Meteor.,* **21,** 1137–1145.

Zipser, E. J., 1977: Mesoscale and convective-scale downdrafts as distinct components of squall-line circulation. *Mon. Wea. Rev.,* **105,** 1568–1589.

——, 1988: The evolution of mesoscale convective systems: Evidence from radar and satellite observations. *Tropical Rainfall Measurements,* J. S. Theon and N. Fugono, Eds., Deepak Publishing, 159–166.